*Geophys. J. Int.* (2007) **171,** 133–144 doi: 10.1111/j.1365-246X.2007.03526.x



# Models of Earth's main magnetic field incorporating flux and radial vorticity constraints

A. Jackson,[1] C. G. Constable,[2] M. R. Walker[3] and R. L. Parker[2]

[1]*Institute for Geophysics, ETH Zürich,* CH-8093 *Switzerland. E-mail: ajackson@ethz.ch*
[2]*IGPP, Scripps Institution of Oceanography, La Jolla,* CA 92093, *USA*
[3]*Department of Public Health, University of Cambridge, UK*

Accepted 2007 June 17. Received 2007 April 14; in original form 2006 December 19

**SUMMARY**

We describe a new technique for implementing the constraints on magnetic fields arising from two hypotheses about the fluid core of the Earth, namely the frozen-flux hypothesis and the hypothesis that the core is in magnetostrophic force balance with negligible leakage of current into the mantle. These hypotheses lead to time-independence of the integrated flux through certain 'null-flux patches' on the core surface, and to time-independence of their radial vorticity. Although the frozen-flux hypothesis has received attention before, constraining the radial vorticity has not previously been attempted. We describe a parametrization and an algorithm for preserving topology of radial magnetic fields at the core surface while allowing morphological changes. The parametrization is a spherical triangle tesselation of the core surface. Topology with respect to a reference model (based on data from the Oersted satellite) is preserved as models at different epochs are perturbed to optimize the fit to the data; the topology preservation is achieved by the imposition of inequality constraints on the model, and the optimization at each iteration is cast as a bounded value least-squares problem. For epochs 2000, 1980, 1945, 1915 and 1882 we are able to produce models of the core field which are consistent with flux and radial vorticity conservation, thus providing no observational evidence for the failure of the underlying assumptions. These models are a step towards the production of models which are optimal for the retrieval of frozen-flux velocity fields at the core surface.

**Key words:** geomagnetism, secular variation, frozen flux.

## 1 INTRODUCTION

Direct observations of the Earth's magnetic field play an important role, alongside palaeomagnetic measurements, dynamo simulations and laboratory experiments, in contributing to our ultimate understanding of the processes which generate and sustain the field over time. Earth's main magnetic field has been modelled repeatedly since the first least-squares models were derived by Gauss, but the advent of vector satellite observations with launching of the Magsat satellite in late 1979 ushered in an era in which high quality geomagnetic data are routinely used to address the problem of obtaining accurate and consistent models of the Earth's main magnetic field at the core–mantle boundary (CMB). Although direct observations do provide the highest resolution images of the field, they remain limited in their resolution, not least because of the presence of the magnetized crust which obscures the shortest wavelength features of the field. Even the most accurate satellite data, currently being provided by the Oersted and Champ satellites, are unable to unequivocally determine the number and locations of patches of opposite polarity flux at the core surface. Such a deficiency was demonstrated neatly, for the case of Magsat data, by O'Brien (1996). Therefore, there remains an unavoidable ambiguity in the images of the field that they can provide.

Beginning with the work of Roberts & Scott (1965), many techniques have been developed over the last 40 yr to produce large-scale maps of the geomagnetic field at the CMB from a given data set. Most adopt a least-squares rationale for fitting the model to the imperfect data, along with some other methodology for making the problem well posed; both models at a particular epoch (e.g. Shure *et al.* 1982; Gubbins & Bloxham 1985; Bloxham *et al.* 1989) and time-dependent models (Bloxham & Jackson 1992; Jackson *et al.* 2000) have successfully been produced using this approach.

The thrust of our paper is to test whether it is possible to construct models of the core magnetic field which satisfy the known constraints which arise when one makes two simplifying assumptions: that the core is a perfect conductor and that the mantle is an insulator. Although these assumptions cannot represent geophysical reality, they are likely to be very good approximations; this prejudice can be used in the geophysical inverse problem to choose from the huge space of models compatible with any particular data set.

We see the construction of these models as a prerequisite to the construction of self-consistent models of fluid flow at the CMB.

The frozen-flux hypothesis is motivated by the differing timescales associated with diffusion and advection in the induction equation, which describes the evolution of the geomagnetic field. The difference is so great that over the time period that one is able to generate field models from direct observations of the magnetic field (*ca*. 400 yr) the diffusive term plays a secondary role and can reasonably be neglected. This in turn implies that the magnetic field lines are frozen to the fluid of the liquid outer core and, therefore, changes in the magnetic field are due solely to advection of the field by the flow. Mapping the field at the CMB also gives partial information on the fluid flow at the CMB.

Adopting the frozen-flux approximation imposes rigorous constraints on resulting field models. Under the frozen-flux approximation, null-flux curves (NFC, curves on which the radial component of the field is zero) are material lines and can neither be created nor destroyed, implying that the topology of field models must be constant throughout time. This means that once a null-flux patch (defined as a patch on the core surface bounded by a NFC) exists it cannot split apart to form two patches, nor can it merge with any other such patch thereby lessening the overall number.

Null-flux patches are subject to additional constraints, namely the constraint of constant integrated flux (Backus 1968) and (when additional approximations are invoked) the radial vorticity constraint (Jackson 1996). The frozen-flux constraint simply states that the flux linked by a patch must be preserved at all times; this is described by eq. (15) below. The vorticity constraint, described in Jackson (1996),[1] requires that the mantle is an insulator so that the radial current vanishes identically at the CMB. Then Kelvin's celebrated circulation theorem applies and the equatorially projected area of a null-flux patch must remain invariant in time. This arises because of the magnetostrophic force balance at the core surface, owing to the very small values of the Ekman and Rossby numbers in the core. Fig. 1 illustrates these ideas schematically.

We make it quite clear at this point that we understand that the preservation of topology is the weakest part of the frozen-flux hypothesis: when two NFCs become very close, it can take a minuscule amount of diffusion for them to merge. That being said, the integrated flux of the merged patch will be the same as the sum of the fluxes of the two original patches, and the same is true of the radial vorticities. Let us clarify that we employ the topological constraints as a necessary vehicle to enable us to keep relevant fluxes and vorticities correct; it is indeed the case that in some of our models flux patches have become so close that it would require only tiny diffusion for them to merge. We do not see this as a problem, since they individually contain the correct fluxes and vorticities. If it is possible to satisfy the constraints whilst preserving topology, it is certainly possible to do so when merging of patches is allowed. In this sense, our strict adherence to the frozen-flux constraints with preserved topology represents the most stringent test of frozen-flux possible.

The frozen-flux approximation was examined in some detail in a series of papers dealing first with estimates of secular variation (Gubbins 1984) and subsequently with the main field (Bloxham & Gubbins 1985, 1986; Gubbins & Bloxham 1985). The problem of developing geomagnetic field models for successive epochs that actually incorporate frozen-flux constraints was first considered by Bloxham & Gubbins (1986). They note two methods for testing the frozen-flux hypothesis: comparison of differences in flux integrals between epochs in light of formal error estimates, and construction of models consistent with the constraints, followed by examination of the degradation in quality of fit to the observations. In applying these tests to data from 1959.5, 1969.5 and 1980 they tentatively concluded that there was evidence for violation of the hypothesis—noting that this result was sensitive to the formal error bars on flux integrals. In an analysis over a longer time interval Bloxham & Gubbins (1985) noted that their core field models evaluated at around 65 yr intervals from 1715 to 1980 were inconsistent with Backus's necessary conditions on the frozen-flux hypothesis. In a later development, Constable *et al.* (1993) enforced the frozen flux constraints by constraining the field model being developed, in this case epoch 1945, to have the same flux patch integrals as a given reference model and minimizing differences from the chosen model. The reference model chosen comprised eight flux patches and was obtained from the Magsat data set, epoch 1980. Constable *et al.* (1993) concluded that the frozen-flux approximation was valid, at least over this interval, since they found models satisfying the constraints (15).

O'Brien *et al.* (1997) provided a more elegant method of enforcing the frozen-flux constraints, when generating field models. They devised an ingenious method for constraining the topology of any field model by the use of inequality constraints; a simple example will illustrate the point. It is crucial that in a patch of negative flux all the field values remain negative everywhere, otherwise nesting of the patch occurs with a patch of positive flux and the topology of the patch is lost. It is this preservation of topology that is the most difficult aspect of the problem to address, at least from a computational standpoint. O'Brien *et al.* (1997) were able to preserve the topology of the patches, but the positions of the patches were prescribed in the modelling process to conform with those in a reference model—once specified they were not allowed to move, and occasional artificial surgical procedures had to be implemented during the modelling. These limitations may not conform to reasonable field behaviour when one considers the kinds of motions that appear to take place with westward drift and other forms of secular variation.

In this paper, we extend the works of Constable *et al.* (1993) and O'Brien *et al.* (1997) (hereafter known as CPS and OCP, respectively) by developing a more flexible algorithm for handling the topological constraints and constructing field models conforming to both the flux and vorticity constraints, defined by eqs (15) and (16). We generate an epoch 2000 reference model, from the high quality Oersted satellite data which has recently been made available, as our starting point for this work. From this we construct four single-epoch models, for the years 1980, 1945, 1915 and 1882, and examine to what extent the frozen-flux approximation is valid over this temporal range by attempting to fit the data satisfactorily, while conforming to both the flux and vorticity constraints. Our results indicate that it is possible to find simple, smooth models of the field which satisfy the required constraints; we therefore, consider that there are no observational grounds for rejecting the frozen flux hypothesis, nor the hypothesis of magnetostrophic balance (which has never been tested before).

The organization of the paper is as follows: Section 2 describes the parametrization of the magnetic field on the core surface, along with the topology preservation algorithm which is the crux of the procedure for easily finding optimal models fitting the data and the constraints. Section 3 describes the reference model, generated

[1] Note a typographical error in Jackson (1996), namely the omission of a minus sign on the right-hand side of eqs (2.9)–(2.11); this does not alter the conclusions.

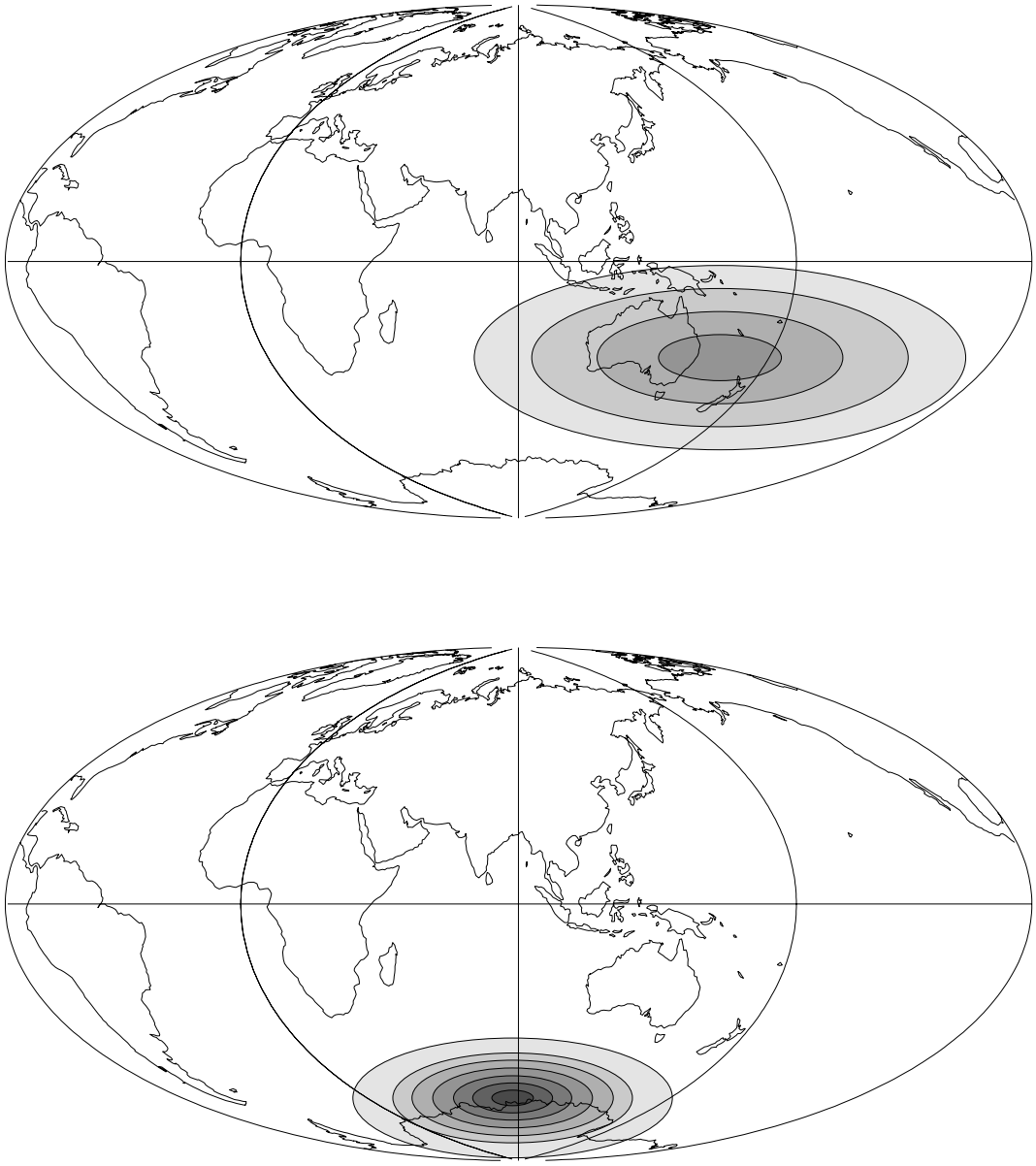

**Figure 1.** Schematic diagram illustrating the conservation of flux and radial vorticity. In this diagram, negative flux is white and the intensity of positive flux is given by grey-shades; the total flux over the surface is zero. A NFC is the line of zero flux, and a null-flux patch is enclosed by that curve. The frozen flux conditions allow a null-flux patch to shrink in size, provided that the flux linked by the patch is preserved. However, the imposition of Kelvin's theorem means the only way that a patch can shrink is to change the latitude of at least part of the patch (bottom panel compared to top).

using the recent Oersted data set, that we use to provide the values of the patch integrals that all other models must achieve. Section 4 describes the results for epochs 1980, 1945, 1915 and 1882.

## 2 MATHEMATICAL FORMULATION

### 2.1 Unconstrained modelling

Much of the mathematical detail is explained in CPS and OCP (to which we refer readers), however below we briefly review their methodology, paying particular attention to modifications we have introduced.

Following CPS, whose notation is followed henceforth, the model $B_r(\hat{\mathbf{s}})$ is defined at a finite set of $N$ nodes on the sphere of unit radius, representing the (normalized) surface of the Earth's core. The nodes are defined by covering the sphere with a tessellation of spherical triangles, generated by bisections and trisections of the regular icosahedron on the unit sphere (Baumgardner & Fredrickson 1985, see fig. 2). This results in an approximately even distribution of spatial nodes over the unit sphere. This representation turns out to be significantly more flexible than the more familiar representation of the field in terms of spherical harmonics (e.g. Langel 1987) and is much more suited to our purposes. For example, under this parametrization the value and sign of the field at a single point is dependent on at most three node values (those adjacent to the point in question) whereas under the spherical harmonic representation the point value depends on the weighted sum of the entire set of model parameters; this leads to considerable difficulties when one wants to constrain the sign of the field at a particular point, one of the operations that we find necessary to perform in what follows.

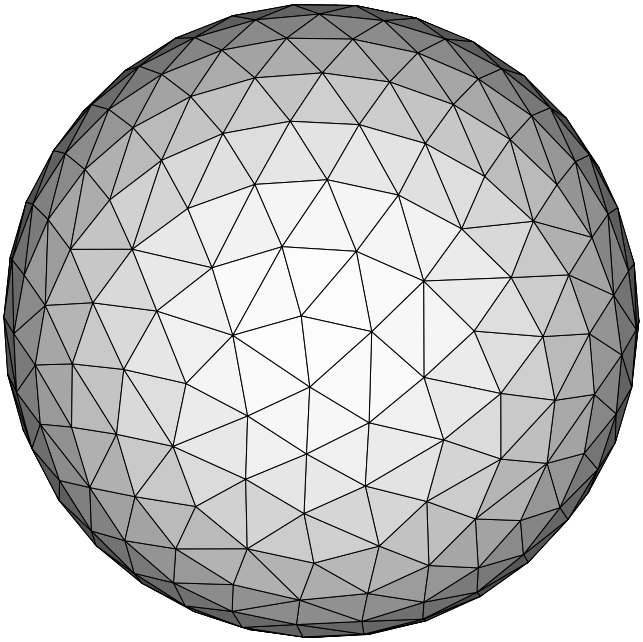

**Figure 2.** The tessellation of the sphere by spherical triangles, generated by bisections and trisections of the regular icosahedron on the unit sphere (Baumgardner & Fredrickson 1985). The planar triangles are shown here for clarity, although the computations take into account the sphericity of the core by using spherical triangles.

The components of the magnetic field **B** at a position **r** outside the core are given by the convolution of the model with the appropriate Green's functions:

$$B_{r,\theta,\phi}(\mathbf{r}) = \int_{\partial C} B_r(\hat{\mathbf{s}}) G_{r,\theta,\phi}(\mathbf{r}, \hat{\mathbf{s}}) d^2\hat{\mathbf{s}}. \tag{1}$$

Here the subscripting $r$, $\theta$, $\phi$ is shorthand for the three spherical components $(r, \theta, \phi)$, $\hat{\mathbf{s}}$ is a position on the core surface, $\partial C$ indicates integration over the core surface and the circumflex denotes a unit vector. $G$ denotes the Green's function which, for each spherical component, is given by

$$G_r(\mathbf{r}, \hat{\mathbf{s}}) = \frac{1}{4\pi}\left[\frac{\rho^2(1-\rho^2)}{R^3} - \rho^2\right], \tag{2}$$

$$G_\theta(\mathbf{r}, \hat{\mathbf{s}}) = -\frac{1}{4\pi}\frac{\rho^3(1+2R-\rho^2)}{R^3 T}(\hat{\mathbf{s}} \cdot \hat{\theta}), \tag{3}$$

$$G_\phi(\mathbf{r}, \hat{\mathbf{s}}) = -\frac{1}{4\pi}\frac{\rho^3(1+2R-\rho^2)}{R^3 T}(\hat{\mathbf{s}} \cdot \hat{\phi}). \tag{4}$$

Here, the core radius $s = 3485$ km, $\rho = s/|\mathbf{r}|$, $\mu = \hat{\mathbf{s}} \cdot \hat{\mathbf{r}}$, $R = \sqrt{1 - 2\mu\rho + \rho^2}$ and $T = 1 + R - \mu\rho$. These Green's functions are derived from the exterior solution to Laplace's equation with Neumann boundary conditions (see CPS for more details)

To generate a continuous representation of the field everywhere, $B_r$ at position **s** within and on the edges of each spherical triangle is defined by linear interpolation of the vertex values, after the triangle is projected onto the plane tangent at its circumcentre using a gnomonic projection (see CPS).

$$\mathbf{s} = \sum_{i=1}^{3} \alpha_i \mathbf{x}_i \quad \text{and} \quad B_r(\mathbf{s}) = \sum_{i=1}^{3} \alpha_i B_r(\mathbf{x}_i), \tag{5}$$

where $B_r$ is defined at vertices $\mathbf{x}_i$ of the spherical triangle, and $\sum_{i=1}^{3} \alpha_i = 1$. A complementary view is that attached to each node is a 2-D tent-like basis function, with five or six planar faces rising to the apex at the node in question (the ambiguity in the number of faces arises from the different number of nearest neighbours resulting from the original tesselation: the 20 nodes of the original icosahedral tesselation have five-fold coordination). Fig. 3 illustrates an example basis function for a five-fold coordinated node, showing the local support. The basis function shows the influence of the model parameter in synthesizing the model: the entire model is generated by summing the basis functions weighted by their node values. In 1-D problems, these basis functions are known as the B-splines of order 2 (see e.g. Lancaster & Salkauskas 1986).

We note that in order for monopoles to be excluded from the model, we must impose the additional constraint

$$\int_{\partial C} B_r d^2\hat{\mathbf{s}} = 0 \tag{6}$$

which would not otherwise be obeyed by an arbitrary model under this parametrization (though note that a model computed with frozen flux constraints imposed (Section 2.2) will automatically fulfill this condition provided the reference model does). We can write the general relationship between a datum $d_j$ at position **r** and the model **b** as

$$d_j = \mathcal{F}_j(\mathbf{b}), \tag{7}$$

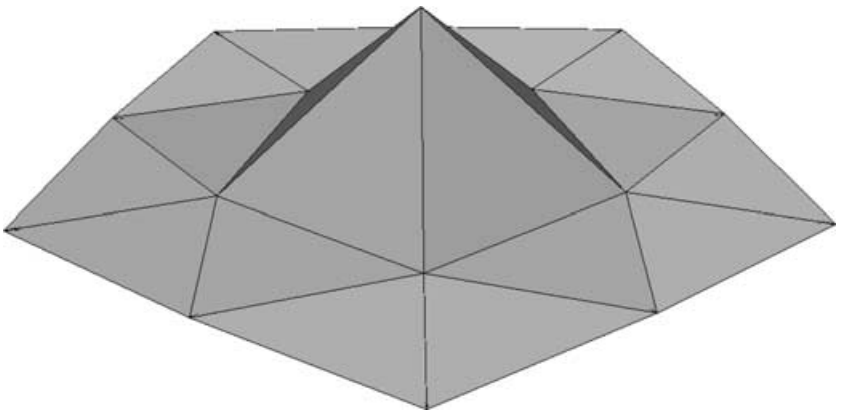

**Figure 3.** The basis function associated with a five-fold coordinated node, illustrated on a small section of a polyhedral rather than a spherical core. The vertical axis shows the amplitude of the basis function; it is zero everywhere apart from in the triangles adjacent to the node to which it is associated. The basis functions are linear 'tent' functions, with value unity at the vertex and zero on the edges. The local support is the key to the efficient computations reported herein.

where $\mathbf{b} = \{b_i\}$ are the $N$ model parameters (i.e. the values of the field at the $N$ nodes) and $\mathcal{F}_j$ represents the forward functional relating the model $\mathbf{b}$ to the datum $d_j$. For the models reported in this paper $N = 812$. In the case of linear data, such as measurements of the $X$, $Y$ or $Z$ components of the field, the relationship between a datum can be written

$$\mathbf{d} = \mathbf{A}\mathbf{b} \tag{8}$$

and A contains the inner products of the appropriate Green's function with the basis functions for each of the node values $b_j$; these form the rows of the so-called design matrix. Inner products for the forward problem (and for the fluxes and radial vorticities) are computed using a weighted sum of samples of the function in the plane triangle, using an optimal degree-5 cubature rule (again, see CPS for more details).

By virtue of the compact support of the basis functions which describe $B_r$, the location of every NFC is defined solely by the values of the nodes which are immediately adjacent to it. Thus finding NFCs requires simply looking for adjacent nodes of opposite sign. This feature is central to the application of inequality constraints which is described in Section 2.2.

Following the standard regularized least-squares methodology (e.g. Parker 1994) we seek a model estimate $\mathbf{b} = \{b_1, b_2, \ldots, b_N\}$ which fits the data $\mathbf{d} = \{d_1, d_2, \ldots, d_M\}$ while minimizing some measure of the model complexity, that is, we seek that $\mathbf{b}$ which minimizes

$$\begin{aligned}\Gamma(\mathbf{b}) &= \sum_{j=1}^{M}\left[\frac{d_j - \mathcal{F}_j(\mathbf{b})}{\sigma_j}\right]^2 + \lambda_s\mathcal{R}(\mathbf{b}) \\ &= [\mathbf{d} - \mathcal{F}(\mathbf{b})]^T\,\mathbf{C}_\mathrm{e}^{-1}\,[\mathbf{d} - \mathcal{F}(\mathbf{b})] + \lambda_s\mathcal{R}(\mathbf{b}).\end{aligned} \tag{9}$$

Here $\sigma_j$ is the uncertainty in $d_j$ which enters the (diagonal) data covariance matrix $\mathsf{C}_\mathrm{e}$. The final term $\mathcal{R}$, describes the model complexity and the damping parameter $\lambda_s$ represents the trade-off between model smoothness and fit to the data: we use $\lambda_s$ to achieve a fit to the data of one standard deviation on average, namely that the misfit

$$\mathcal{M} = \sqrt{\frac{1}{M}\sum_{j=1}^{M}\left[\frac{d_j - \mathcal{F}_j(\mathbf{b})}{\sigma_j}\right]^2} \tag{10}$$

has the value unity. The numbers of data ($M$) for the different data sets used are given in Section 4. In what follows, we adopt the $\mathrm{F}_4$ norm of Shure *et al.* (1982) as our regularization; we minimize the squared horizontal gradient of the radial component of the field, integrated over the core surface:

$$\mathcal{R} = F_4(B_r) = \int_{\partial C} |\nabla_\mathrm{h} B_r|^2 d^2\hat{\mathbf{s}} = \mathbf{b}^T\mathbf{C}_\mathrm{m}^{-1}\mathbf{b} \tag{11}$$

(Other forms of $\mathcal{R}$ could equally well have been used, for example, the Ohmic heat norm or the dissipation norm: qualitatively the same result would be obtained.) For more details on the evaluation of $\mathcal{R}$ see CPS.

In (9) the fit to the data is measured by the squared misfit, a commonly used criterion for discriminating between models (see the discussion in Parker 1994). This would also be a maximum likelihood estimator if the errors contaminating the data set were to originate from a Gaussian distribution. However, we caution that there is accumulating evidence that the distribution of errors may be far from Gaussian (e.g. Walker & Jackson A. 2000). Nevertheless, bearing this cautionary note in mind we shall proceed with the least-squares approach. In general $\mathcal{F}$ is non-linear so an iterative approach is employed: $\mathcal{F}$ is linearized about an estimate of the solution $\mathbf{b}^k$, where the superscript denotes the $k$th estimate, and then (9) is solved for an estimate $\mathbf{b}^{k+1}$:

$$\mathbf{b}^{k+1} = \left(\mathbf{A}^T\mathbf{C}_\mathrm{e}^{-1}\mathbf{A} + \lambda_s\mathbf{C}_\mathrm{m}^{-1}\right)^{-1}\mathbf{A}^T\mathbf{C}_\mathrm{e}^{-1}\left[\mathbf{d} - \mathcal{F}(\mathbf{b}^k) + \mathbf{A}\mathbf{b}^k\right], \tag{12}$$

where A is the matrix of derivatives of the data with respect to the model at the $k$th iterate. As in OCP we use the Newton algorithm variant that solves for the vector $\mathbf{b}^{k+1}$, rather than a perturbation $\boldsymbol{\delta}\mathbf{b}$ to $\mathbf{b}^k$, in order that inequality constraints (which apply to $\mathbf{b}^{k+1}$ and not to $\boldsymbol{\delta}\mathbf{b}$) can be imposed. The linear system is actually solved using the QR algorithm, which obviates the need to generate the normal equations $\mathsf{A}^T\mathsf{C}_\mathrm{e}^{-1}$ A; the QR version (Lawson & Hanson 1995) of the system is passed to the algorithm Bounded Variable Least Squares (BVLS) (see Section 2.2 and OCP) when constraints are imposed. Clearly for linear data the terms $\mathcal{F}(\mathbf{b}^k)$ and $\mathsf{A}\,\mathbf{b}^k$ cancel, but, somewhat surprisingly, this is also the case for $H$ and $F$ intensity data, illustrating that the non-linearity is very slight for these data. We illustrate this for $H$, but a similar relation follows for $F$:

$$\frac{\delta H}{\delta b_i} = H^{-1}\left(X\frac{\delta X}{\delta b_i} + Y\frac{\delta Y}{\delta b_i}\right) \tag{13}$$

so

$$\begin{aligned}\mathbf{A}\mathbf{b}^k &= \frac{\delta H}{\delta b_i}b_i = H^{-1}\left(X\frac{\delta X}{\delta b_i}b_i + Y\frac{\delta Y}{\delta b_i}b_i\right) = H^{-1}(X^2 + Y^2) \\ &= H = \mathcal{F}(\mathbf{b}^k).\end{aligned} \tag{14}$$

The iterative procedure continues until a converged solution is obtained (the end of Section 2.2 gives exact criteria). For all non-linear data we work with the true magnetic elements ($X, Y, Z, H, F, I, D$), rather than the linear Bauer (1894) representation of $I$ and $D$ employed by OCP and CPS. This is because the flux and radial vorticity constraints (see below) imposed on the model result in the problem being non-linear; we found that the additional non-linearity due to $I$ and $D$ caused little extra computational expense.

### 2.2 Constrained modelling

The frozen-flux approximation (Roberts & Scott 1965) has some severe consequences on the magnetic field at the core surface. Since diffusion is neglected, NFCs (curves on which the radial magnetic field $B_r = 0$) cannot connect or break, thus implying that the topology of the field must be preserved throughout time. Further to this there are constraints on each patch (defined by the region on the core surface enclosed by a NFC) which must also be preserved throughout time; namely the flux constraint (Backus 1968) and the radial vorticity constraint (Jackson 1996).

The flux and vorticity constraints are given by

$$\mathcal{B} = \frac{d}{\mathrm{d}t}\int_{S_j} B_r\; d^2\hat{\mathbf{s}} = 0 \tag{15}$$

$$\mathcal{V} = \frac{d}{\mathrm{d}t}\int_{S_j} \cos\theta\; d^2\hat{\mathbf{s}} = 0, \tag{16}$$

respectively, where $S_j$ is the region bound by a NFC and $\theta$ is the co-latitude. Eq. (15) is well known, and originates from Backus (1968); we do not discuss its origins further. Eq. (16) is perhaps less-well known, and originates from Jackson (1996). It originates from a treatment of the Navier–Stokes equation in the so-called magnetostrophic limit, in which inertial and viscous forces have been dropped on account of the small Rossby and Ekman numbers in the core. The Navier–Stokes equation reads

$$2\rho\boldsymbol{\Omega}\wedge\mathbf{u} = -\nabla p + \rho'\mathbf{g} + \mathbf{J}\wedge\mathbf{B}, \tag{17}$$

where $\mathbf{u}$ is the fluid velocity, $\Omega$ is the rotation vector, $\rho$ is the density, $p$ is the pressure, $\rho'$ is the density perturbation associated with convection and $\mathbf{J}$ is the electrical current density. When integrals of the radial part of the curl of the left-hand side over null-flux patches are considered, all contributions from the pressure, buoyancy and Lorentz force on the right-hand side vanish. The vanishing of the Lorentz force contribution occurs because we have chosen NFCs as boundaries of the regions of integration. Despite the fact that the fluid moves magnetostrophically in general, the NFCs actually move geostrophically by dint of the fact that the Lorentz force vanishes identically on these curves. This, coupled with the fact that the NFCs are material lines, leads to eq. (16).

The veracity of eq. (16) cannot be ensured. The dismissal of the viscous force is correct in the main body of the core, but the fluid must obey non-slip boundary conditions at the CMB, and will form some type of viscous boundary layer. We have assumed that the constraint holds beneath the viscous (or magnetic) boundary layer, across which the radial component of $\mathbf{B}$ is continuous (this is required in the proof), but the issue is a delicate one on which we will not dwell. A similar unanswered question concerns the continuity of the horizontal components of $\mathbf{B}$ across the viscous (or magnetic) boundary layer.

To enforce eqs (15) and (16) we follow CPS (who only consider constraint eq. 15) and define a reference model, $\mathbf{b}^*$ say, which designates the number of patches, $P$, to be preserved, together with the flux and vorticity associated with each patch. This gives us a set of $P$ target fluxes and a set of $P$ target vorticities which any epoch model estimate must match. In enforcing constraints (15) and (16) on the model estimate, the function (9) is expanded to the problem of minimizing

$$\begin{aligned}\Gamma(\mathbf{b}) = &\sum_{j=1}^{M}\left[\frac{d_j - \mathcal{F}_j(\mathbf{b})}{\sigma_j}\right]^2 + \lambda_s\mathcal{R}(\mathbf{b}) \\ &+ \lambda_f \sum_{j=1}^{P}\left[\mathcal{B}_j(\mathbf{b}) - \mathcal{B}_j(\mathbf{b}^*)\right]^2/\mathcal{B}_j(\mathbf{b}^*) \\ &+ \lambda_v \sum_{j=1}^{P}\left[\mathcal{V}_j(\mathbf{b}) - \mathcal{V}_j(\mathbf{b}^*)\right]^2/\mathcal{V}_j(\mathbf{b}^*). \end{aligned} \tag{18}$$

Here $\lambda_f$ and $\lambda_v$ are parameters defining how well constraints eqs (15) and (16) are enforced; values of $10^{10}$ have been used. For example, $\lambda_f = 0$ implies that eq. (15) is not enforced, while $\lambda_v = 0$ implies (16) is not enforced. Eqs (15) and (16) are implemented via quadratic constraints in eq. (18), and therefore, $\mathcal{B}_j(\mathbf{b}^*)$ and $\mathcal{V}_j(\mathbf{b}^*)$ can be thought of as $2P$ additional 'data', supplied by the reference model, and the 'forward function' for each of the $2P$ 'data' is made up of a suitably weighted vector, describing the contribution of the nodes within patch $S_j$ to its flux or vorticity integral. Note that we have chosen to implement the constraints as a penalty on the relative difference between the current model and the reference model. This ensures that all constraints are satisfied to the same small percentage error. Without this device, it is possible for the largest fluxes and vorticities to be preferentially fit at the expense of the smallest.

In order to optimize the system (18) we use a Newton algorithm. For the linear data we use the matrix linking the data to the model parameters, and for the non-linear data we use the Frechét derivatives of the data with respect to the model parameters. For the patch integrals we need the derivatives with respect to perturbations in the model. Consider the general integral

$$I = \int_{\mathbf{x}=f(\mathbf{b})} g(\mathbf{b},\theta,\phi)\,\mathrm{d}S. \tag{19}$$

Then the derivative is in general

$$\delta I = \int_{\mathbf{x}=f(\mathbf{b})} \delta g(\mathbf{b},\theta,\phi)\,\mathrm{d}S + \oint_{\mathbf{x}=f(\mathbf{b})} g(\mathbf{b},\theta,\phi)(\boldsymbol{\delta}\mathbf{x}\cdot\hat{\mathbf{n}})\,\mathrm{d}l, \tag{20}$$

where $\boldsymbol{\delta}\mathbf{x}\cdot\hat{\mathbf{n}}$ is the component of the perturbation of the boundary in the direction $\hat{\mathbf{n}}$ normal to the boundary due to a change in the model. We find

$$\boldsymbol{\delta}\mathbf{x}\cdot\hat{\mathbf{n}} = -\frac{\delta B_r}{|\nabla_{\mathrm{h}} B_r(\mathbf{r})|} \tag{21}$$

for both our integrals where the boundaries are the NFCs. Although the null-flux integrals (eq. 15) are non-linear, it is a felicitous fact that a perturbation $\delta\mathcal{B}$ can be related to a perturbation in the model $\delta\mathbf{b}$ as

$$\delta\mathcal{B} = \mathbf{B}\delta\mathbf{b} \tag{22}$$

with no approximation at all by virtue of the fact that the boundary terms in the perturbation of eq. (15) vanish (Bloxham & Gubbins 1985). This is not the case for the Frechét derivatives of $\mathcal{V}_j$ with respect to the $b_i$, for which the boundary integral is the only non-vanishing contribution.

The system is solved by iterating to a converged solution using a BVLS algorithm to find a field model which retains the topology of the given reference model, $\mathbf{b}^*$ (described in Section 2.3). We omit a description of the methodology of BVLS here and refer readers to Lawson & Hanson (1995) and Stark & Parker (1995) who give a lucid description of the method. With the topological constraints satisfied we are able to enforce constraints eqs (15) and (16) by choosing $\lambda_f$ and $\lambda_v$, appearing in eq. (18), such that a desired conformity is achieved. The final converged model is such that both the normalized misfit and model complexity ($\mathcal{R}$) have converged, the model fits the data satisfactorily, and the average percentage error (averaged over the $P$ patches) of the flux and vorticity constraints is less than 1 per cent.

### 2.3 Topology preservation

At the heart of our optimization procedure is an algorithm to retain topology of a model from iteration to iteration while allowing changes in morphology. Topology preservation ensures that the number and nestedness of patches remains the same; morphological changes are allowed, so that patches can change their shape, size and location.

The concept of neighbours is central to the algorithm. Under the icosahedral discretization the coordination (or the number of nearest-neighbours) of any node is either six- or five-fold (the former being overwhelmingly the more common). The 'sign' of a node is the sign of the value of $b_i$ at that node. At any one iteration only certain nodes are allowed to change sign from their current values. The nodes which are allowed to change sign form the 'unconstrained set' $\mathcal{U}$, and the nodes which are not allowed to change sign form the 'constrained set' $\mathcal{C}$. All variables are assigned upper and lower bounds $\mathbf{u}$ and $\mathbf{l}$ so that $l_j \le b_j \le u_j$. The constrained set are assigned upper and lower bounds in the following way:

$$\begin{aligned}&\text{If} \quad b_j \in \mathcal{C} \quad \text{and} \quad b_j < 0 \text{ then } l_j = -|\aleph|;\ u_j = -|\epsilon| \\ &\text{If} \quad b_j \in \mathcal{C} \quad \text{and} \quad b_j > 0 \text{ then } l_j = |\epsilon|;\ u_j = |\aleph|,\end{aligned} \tag{23}$$

where in our application we have set $\epsilon = 10$ and $\aleph = 10^4$ μT, though in reality the upper bounds are generally impotent because of the regularization of the model that is applied.

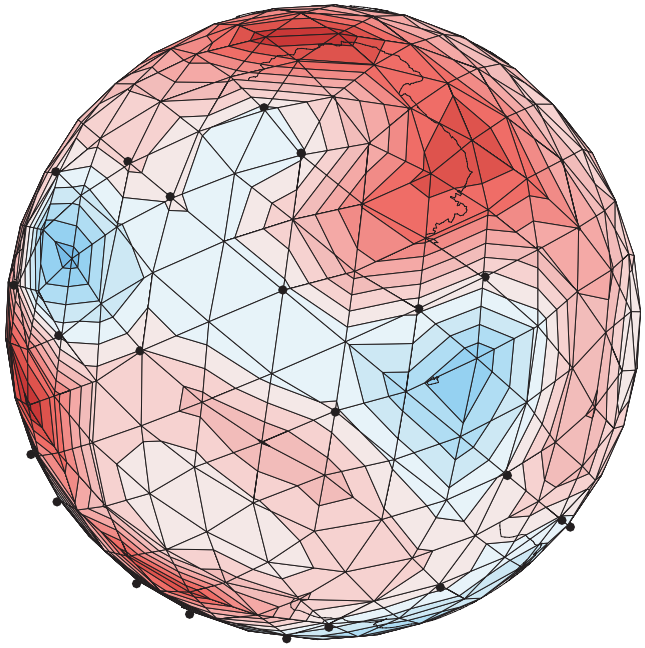

**Figure 4.** The assignment of nodes to the sets $\mathcal{U}$ (unconstrained) and $\mathcal{C}$ (constrained), the sets where signs of the nodes are either free to change sign or must remain of the current sign, respectively. The assignments ensure that the topology of null-flux patches is retained. Shown here is an example with nodes which are free to change sign coloured black; all others must retain their current sign.

Only nodes whose radial field value is close to zero are likely to usefully change sign, so on any one NFC $\partial S$ we begin by ranking adjacent nodes in terms of their proximity to $\partial S$. Once the ordered list has been made we move down the list, assigning to $\mathcal{U}$ each node sequentially, provided it satisfies a set of 'topology rules'. We distinguish between 'inside' and 'outside' the patch (the distinction, although arbitrary, can be definitely assigned). We give an example in Fig. 4 of the unconstrained nodes at a particular iteration of a model. The nodes marked with black dots are unconstrained, and are free to change sign. All other nodes must retain their current sign. The figure illustrates the most important topology rule: if a node is an interior node then it is prevented from being assigned to $\mathcal{U}$ if any exterior neighbour is already in $\mathcal{U}$ (and vice versa). This prevents the creation of new null-flux patches. There are a considerable number of more elaborate rules designed to deal with patches containing very small numbers of nodes; a comprehensive list of the rules is detailed in the Appendix. As an example, there should be more than one node within any patch at any time. A patch containing only one node would necessarily always have that node's sign constrained (to prevent the patch disappearing) but this means that the patch cannot migrate without first enlarging. Problems such as this one can be eliminated by increasing the resolution of the model.

The algorithm works extremely effectively: patches can migrate easily across the core from iteration to iteration; changes in size and shape are accomplished smoothly as the model vector is updated.

## 3 THE REFERENCE MODEL

The reference model, $\mathbf{b}^*$ is generated from a subset of the high quality Oersted data set described in Olsen *et al.* (2000). The data set comprises 3907 vector triples $(B_r, B_\theta, B_\phi)$ together with 2148 total field intensity measurements, $F$, spanning an interval of approximately 4 months around epoch 2000. Using the secular variation estimate of the IGRF we reduced the data to epoch 2000 and, furthermore, we remove the Dst-dependent external magnetic field model of Olsen *et al.* (2000). Finally, following OCP, we decimate the resulting data into 5° cells in order to remove any possible error correlation due to crustal noise. This results in a final data set of 1228 vector triples and 998 scalar measurements with excellent global coverage.

Associated with each data measurement is an error estimate and, following Olsen *et al.* (2000), we allow for 2.25 nT in the scalar measurements $F$. Holme & Bloxham (1996) describe a method in which the vector triples $(B_r, B_\theta, B_\phi)$ are rotated to a new coordinate system $(B_B, B_\perp, B_3)$, where $B_B$ is in the direction of the field $\mathbf{B}$ at the data coordinate, and $B_\perp, B_3$ are in the directions $\hat{\mathbf{n}} \wedge \mathbf{B}$ and $\mathbf{B} \wedge (\hat{\mathbf{n}} \wedge \mathbf{B})$, respectively. With respect to the Oersted data $\hat{\mathbf{n}}$ represents a unit vector in the direction of the stellar imager (SIM) bore-sight (Olsen *et al.* 2000). In this new rotated coordinate system the errors on the field components $(B_B, B_\perp, B_3)$ are uncorrelated. Following Holme & Bloxham (1996) $(B_B, B_\perp, B_3)$ are assigned weightings defined by the parameters $\chi$ and $\psi$, together with the field strength $|\mathbf{B}|$. We set $\chi = 60''$, $\psi = 10''$, see Olsen *et al.* (2000).

In Fig. 5 we illustrate $\mathbf{b}^*$ resulting from the Oersted data, plotted at the core surface $s = 3485$ km. We implement a clamping scheme to make the least-squares method insensitive to outliers: final iterations are performed rejecting data whose residuals exceed 3 standard deviations. The normalized misfit $\mathcal{M}$ of the model is 1.01 and the number of data rejected is 26 vector triples and 171 scalar measurements. Although this may seem quite a large number of rejected $F$ data, we account for this by the fact that topological constraints (eight patches) are enforced on the model, so as to make direct comparisons with the work of CPS. (If the topological constraints are removed a reference model can be found with misfit of 1.01; in this case only 40 $F$ data are rejected, however the model comprises 11 patches.) The flux strengths and vorticities of each patch, together with a description of their position, can be found in Tables 1(a) and (b), where we use the same patch identification as CPS. Comparing Fig. 5 with the 1980 reference model of CPS (therein called STT1980) we see that the reference models are similar, although $\mathbf{b}^*$ is slightly rougher than STT1980 (also indicated by the flux integrals of $\mathbf{b}^*$ (Table 1a) being of greater magnitude). We find this to be the case for our own models for 2000 and 1980, see Table 2. This is to be expected as the Oersted data are of higher quality than those used by CPS (Magsat data) when developing STT1980.

## 4 RESULTS

We now proceed to investigate whether it is possible to generate field models consistent with the epoch 2000 reference model $\mathbf{b}^*$, described above. If we are able to obtain such models which, while fitting the data adequately, satisfy both the flux and vorticity constraints, then we are in a strong position to state that the frozen flux approximation of Roberts & Scott (1965) is valid, at least over the timescale considered in this paper.

We investigate the validity of the frozen flux approximation over five epochs; namely 2000 (which provides the reference patch integrals), 1980, 1945, 1915 and 1882. The 1980 Magsat data set is described in detail in OCP, to which we refer readers for more details. Here we merely state that the data are linear and comprise 1262 $X$, 1262 $Y$ and 1654 $Z$ measurements. The data set for 1945 comprises observatory and survey data and is described in detail in CPS; briefly the data are made up of 555 $X$, 554 $Y$, 634 $Z$ and

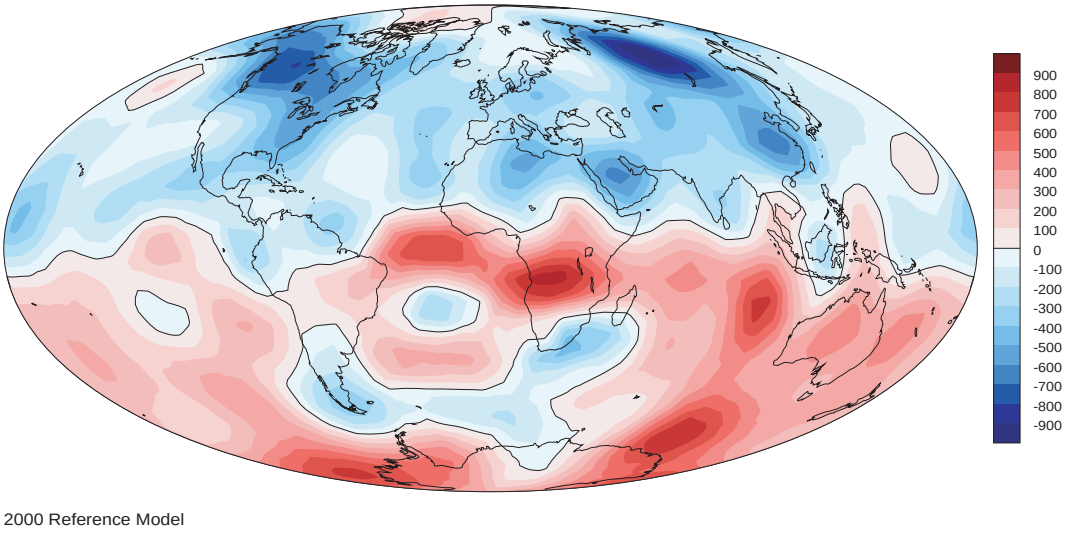


**Figure 5.** The reference model $\mathbf{b}^*$, epoch 2000, plotted on the core surface, radius $s = 3485$ km. Red colours indicate flux out of the core, blue contours are flux into the core; the contour interval is 100 μT. Misfit = 1.01, $\mathcal{R} = 0.484$ μT km$^{-1}$. Aitoff equal area projection. All models in this paper have used $N = 812$ nodes.

**Table 1a.** Fluxes, in μT, of the topologically constrained models. Epoch 2000 defines the reference model, $\mathbf{b}^*$.

| Patch | Position | Epoch | | | | |
|---|---|---|---|---|---|---|
| | | 2000 | 1980 | 1945 | 1915 | 1882 |
| 1 | N. pole | 53.77 | 53.77 | 53.77 | 53.82 | 53.77 |
| 2 | N. hemisphere | −17 566 | −17 565 | −17 573 | −17 350 | −17 561 |
| 3 | Bone | −1317.5 | −1317.9 | −1316.3 | −1310.6 | −1316.4 |
| 4 | S. hemisphere | 18 932 | 18 933 | 18 940 | 18 709 | 18 926 |
| 5 | Easter Island | −21.66 | −21.66 | −21.84 | −21.66 | −21.66 |
| 6 | W. Pacific | 27.95 | 27.68 | 26.88 | 27.94 | 28.12 |
| 7 | St. Helena | −143.51 | −143.34 | −143.42 | −143.35 | −143.55 |
| 8 | E. Pacific | 34.55 | 34.31 | 34.34 | 34.33 | 34.31 |

**Table 1b.** Vorticities, in steradian, of the topologically constrained models. Epoch 2000 defines the reference model, $\mathbf{b}^*$.

| Patch | Position | Epoch | | | | |
|---|---|---|---|---|---|---|
| | | 2000 | 1980 | 1945 | 1915 | 1882 |
| 1 | N. pole | 0.079 | 0.079 | 0.079 | 0.079 | 0.079 |
| 2 | N. hemisphere | 2.916 | 2.916 | 2.916 | 2.916 | 2.916 |
| 3 | Bone | −0.559 | −0.559 | −0.559 | −0.558 | −0.557 |
| 4 | S. hemisphere | −2.445 | −2.445 | −2.445 | −2.445 | −2.446 |
| 5 | Easter Island | −0.017 | −0.017 | −0.017 | −0.017 | −0.017 |
| 6 | W. Pacific | 0.032 | 0.032 | 0.032 | 0.032 | 0.032 |
| 7 | St. Helena | −0.032 | −0.032 | −0.032 | −0.032 | −0.032 |
| 8 | E. Pacific | 0.024 | 0.024 | 0.024 | 0.024 | 0.024 |

322 *D* measurements. The data distribution is poor in contrast to the satellite data as it is confined to land based measurements (see figs 3–5 of CPS). However, this gives us a good opportunity to study the effect of differing data coverage on the constrained modelling. The 1915 data set is derived from the 20th century historical database described in Bloxham *et al.* (1989), and contains a considerable amount of oceanic data from the ship *Carnegie*. The data set comprises 1156 *X*, 1021 *Y*, 1455 *Z*, 628 *H*, 173 *I* and 1394 *D* data. Finally, the data set for 1882 is the one used in Walker & Jackson (2000) and comprises approximately 10 000 observations with reasonably global coverage (see fig. 2 of Walker & Jackson 2000).

**Table 2.** Comparison of model misfits and roughnesses.

| Model | Misfit $\mathcal{M}$ | Roughness $\mathcal{R}$ |
|---|---|---|
| 2000 | 1.010 | 0.484 μT km$^{-1}$ |
| 1980 | 0.994 | 0.431 μT km$^{-1}$ |
| 1945 | 0.973 | 0.337 μT km$^{-1}$ |
| 1915 | 0.976 | 0.325 μT km$^{-1}$ |
| 1882 | 1.071 | 0.370 μT km$^{-1}$ |

**Table 3.** Rules for assigning a node to $\mathcal{U}$ or $\mathcal{C}$. $\#n_j^{(b)}$ is the number of boundary neighbours and $\#n_j^{(h)}$ the number of hinterland neighbours. (see appendix).

| $\#n_j^{(b)}$ | $\#n_j^{(h)}$ | Assignment |
|---|---|---|
| 1 | 0 | $\mathcal{U}$ |
| 2 | 0 | $\mathcal{C}$ |
| 2 | 1, 2 | $\mathcal{U}$ |
| 3, 4, 5 | 0 | $\mathcal{C}$ |

In Fig. 6, we illustrate the radial component of the Earth's magnetic field, plotted at the core mantle boundary, for epoch 1980, constrained by $\mathbf{b}^*$. Comparing Figs 5 and 6, we see that they are remarkably similar; a fact which is reassuring for two reasons. First both models are generated from high quality data with excellent global coverage and second, and more importantly, the two models are only 20 yr apart. The observable differences between the two models are fairly small scale, for example, the slight change in the negative flux patch over the Antarctic. The reference model $\mathbf{b}^*$ is slightly rougher than epoch 1980; this is to be expected as the data from Oersted is of a higher quality (smaller error budget) than that of the Magsat mission. Comparing fluxes (Table 1a) and vorticities (Table 1b) of epoch 1980 with $\mathbf{b}^*$ we see that they give excellent agreement, indicating that the frozen flux approximation is valid over this short period. Comparing Fig. 6 with STT1980 of CPS we see that they are in good agreement, although Fig. 6 is slightly rougher than STT1980 due to the stronger constraints placed on each patch.

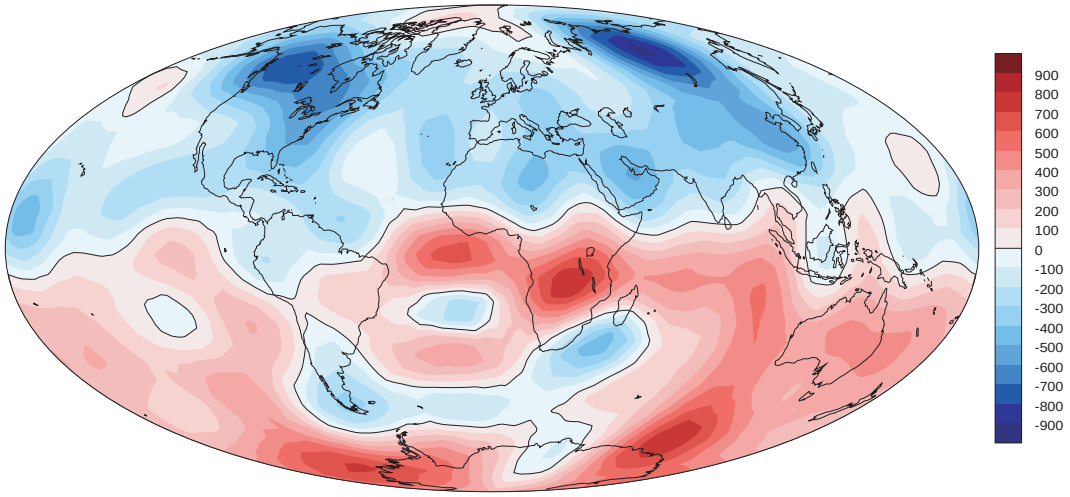


**Figure 6.** The 1980 constrained field model, plotted on the core surface. Colours as in Fig. 5. Misfit = 0.994, $\mathcal{R} = 0.431$ μT km$^{-1}$.

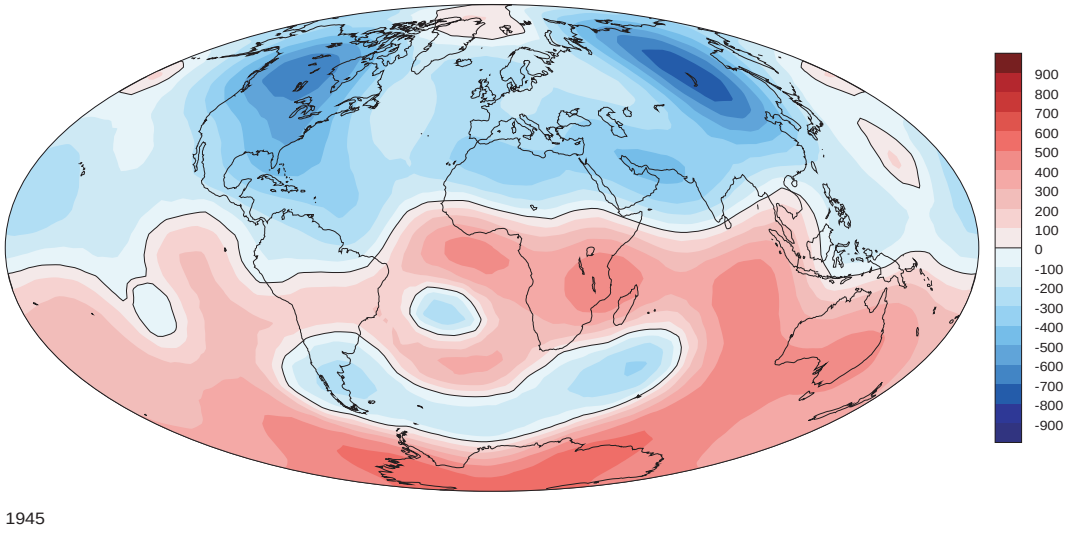


**Figure 7.** The 1945 constrained field model, plotted on the core surface. Colours as in Fig. 5. Misfit = 0.973, $\mathcal{R} = 0.337$ μT km$^{-1}$.

Fig. 7 illustrates the model estimate for epoch 1945. Comparing with $\mathbf{b}^*$ we first note how much smoother the model is, as shown by the value of $\mathcal{R}$ for the two models. This is because the data is confined to land based observations, thus giving a much poorer global coverage than the satellite data used to construct the reference model. However, even with the contrast in model complexities, we are able to produce a model for epoch 1945 satisfying both the flux and vorticity constraints of $\mathbf{b}^*$, see Tables 1a and b. Readers might be concerned that visually the patch fluxes in Figs 5 and 7 appear not to be conserved [e.g. compare the positive (red) southern hemisphere patches]; rest assured that this is not the case. The large peaks in magnetic field strength are more localized in Fig. 5, whereas in Fig. 7 they have been smoothed out over a greater area. The net effect is to conserve the flux, as illustrated in Table 1a, but to the naked eye the models may look somewhat misleading. The main difference between the morphology of the two field models is in patch 3, the 'Bone' in the southern hemisphere. We feel that this is a consequence of the contrast in data distributions over the southern region, rather than an effect due to the constraints imposed on the system.

Figs 8 and 9 illustrate the model estimates for epochs 1915 and 1882, respectively. Comparing all the plots we see that patches 5 and 7 (Easter Island and St. Helena) remain fairly stationary throughout time, whereas patches 6 and 8 (W. and E. Pacific) are much more active, changing both their latitude and longitude throughout time. The two large negative regions of flux within patch 1 (N. Hemisphere) are approximately independent of longitude in all epoch models, although the region over Canada does drift down into North America as we track back in time. This effect was also found in the unconstrained, time dependent, model of Jackson *et al.* (2000). Finally, we note that, once again, the epoch models for 1915 and 1882, whilst fitting the data satisfactorily, conform to both the flux and vorticity constraints.

Table 2 summarizes the characteristics of the model. We find that all the models have less complexity, measured by the roughness $\mathcal{R}$, than the reference model. This is precisely what we would hope, since none of the data sets have the resolving power of the reference model data set. This point is reinforced in Fig. 10, which shows the Lowes magnetic energy spectrum of the field, as a function of spherical harmonic degree. None of the models with constraints require

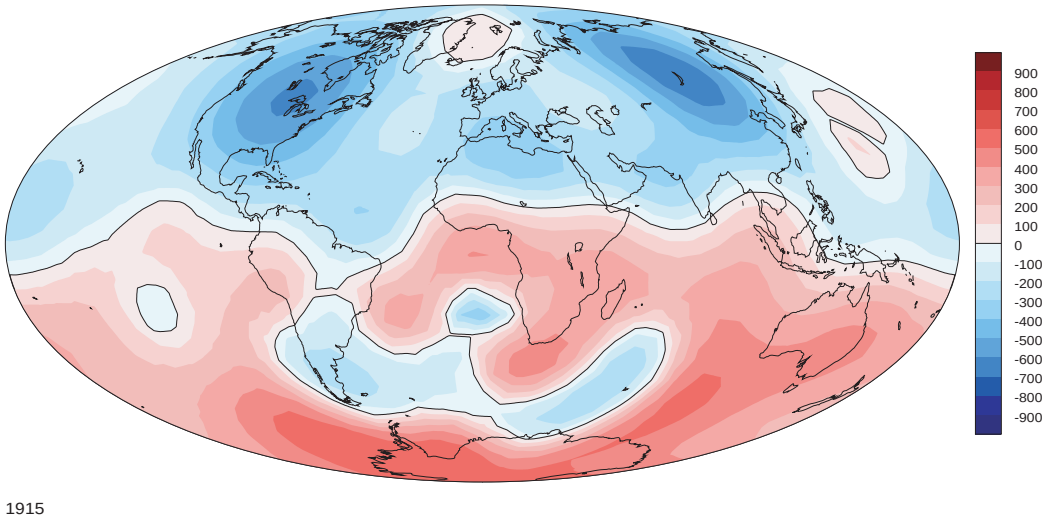


**Figure 8.** The 1915 constrained field model, plotted on the core surface. Colours as in Fig. 5. Misfit = 0.976, $\mathcal{R} = 0.325$ μT km$^{-1}$.

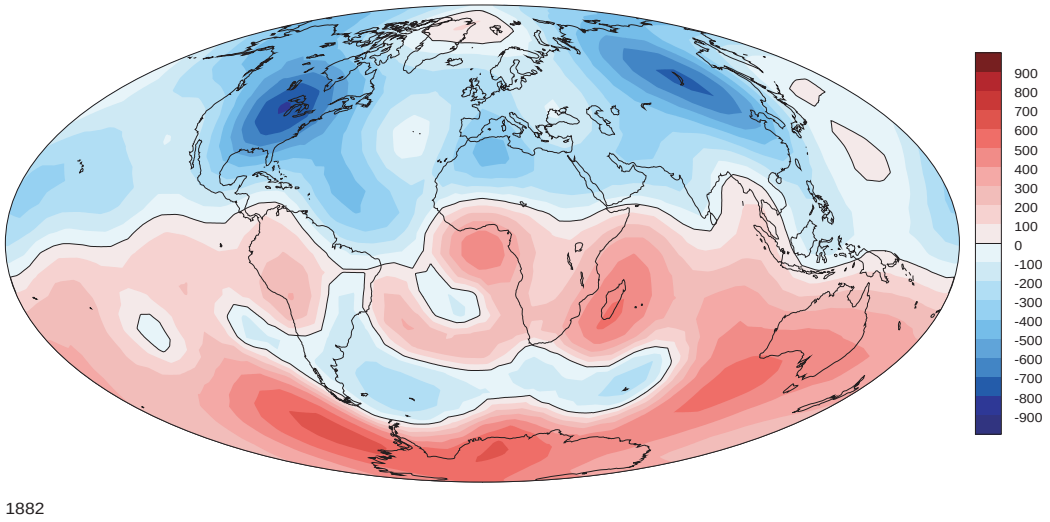


**Figure 9.** The 1882 constrained field model, plotted on the core surface. Colours as in Fig. 5. Misfit = 1.071, $\mathcal{R} = 0.370$ μT km.

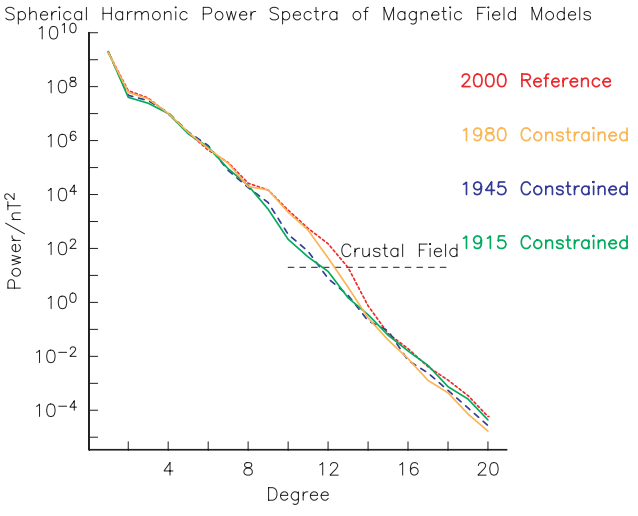


**Figure 10.** Comparison of spherical harmonic energy spectra (Lowes spectra) for the unconstrained and constrained models.

more energy than the 2000 reference model, and the imposition of the constraints does not affect their smooth decay of power with degree $l$.

## 5 CONCLUSIONS

The main result of the paper is that we find no insuperable difficulties in calculating models for the last century which are consistent with the frozen-flux hypothesis. This is encouraging, since theoretically we expect the core's behaviour to be well approximated in this way. Recent dynamo calculations support this view: both Roberts & Glatzmaier (2000) and Rau *et al.* (2000) find that the frozen flux hypothesis is a useful one, though their approaches are different. Roberts & Glatzmaier (2000) analyse the unsigned flux, which is the sum of all the fluxes through the null-flux patches considered here, but without regard to sign; it is constant for a frozen-flux core. They find that over a 150 yr time span the change in the unsigned flux is only 3 per cent, which they understandably consider to be small. Rau *et al.* (2000) test their ability to recover velocity fields from dynamo calculations under the frozen-flux approximation, and again find a fair degree of success in doing so. In these calculations the magnetic Reynolds number (the ratio of diffusive to advective

timescales) is between 100 and 300, possibly slightly low for the core.

Many attempts have been made to recover the fluid flow at the CMB from surface observations, for comparison with dynamo models, and for calculations of core angular momentum and core-mantle coupling. With occasional exceptions (e.g. Waddington *et al*. 1995), these calculations are performed by using models of global geomagnetic main field and secular variation as the 'data' for the inversion. Although diffusive theories exist, the vast majority of methods for inverting for fluid flow at the CMB are based on the frozen-flux hypothesis. Therefore, we see the models we have developed herein as a logical step towards the self-consistent derivation of fluid motions (i.e. the fluid motions are based on models which are consistent with the assumptions required by the fluid motion inversion). In the future we will report on the calculation of time-dependent magnetic field models that satisfy the same constraints as in the present paper.

## ACKNOWLEDGMENTS

This work was supported by NERC grant number GR3/11489, NASA Grants NAG5-2968 and NAG5-3932 and the Royal Society of London. This work was begun when AJ was a visitor at Scripps Institution of Oceanography; AJ thanks members of IGPP for the generous hospitality shown and the Green Foundation for support of his visit. We thank John Woodhouse for valuable advice at a very early stage of this project. This is Institut für Geophysik contribution number 1504.

## REFERENCES

Backus, G.E., 1968. Kinematics of geomagnetic secular variation in a perfectly conducting core, *Phil. Trans. R. Soc. Lond., A,* **263,** 239–266.

Bauer, L.A., 1894. An extension of Gaussian potential theory of terrestrial magnetism, *Proc. Am. Ass. Adv. Sci.,* **43,** 55–58.

Baumgardner J. & Fredrickson, P.O., 1985. Icosahedral discretization of the two-sphere, *SIAM J. Num. Anal.,* **22,** 1107–1115.

Bloxham, J. & Gubbins, D., 1985. The secular variation of Earth's magnetic field, *Nature,* **317,** 777–781.

Bloxham, J. & Gubbins, D., 1986. Geomagnetic field analysis—IV. Testing the frozen-flux hypothesis, *Geophys. J. R. Astr. Soc.,* **84,** 139–152.

Bloxham, J., Gubbins, D. & Jackson, A., 1989. Geomagnetic secular variation, *Phil. Trans. R. Soc. Lond., A,* **329,** 415–502.

Bloxham, J. & Jackson, A., 1991. Fluid flow near the surface of the Earth's outer core, *Rev. Geophys.,* **29,** 97–120.

Bloxham, J. & Jackson, A., 1992. Time dependent mapping of the magnetic field at the core-mantle boundary, *J. geophys. Res.,* **97,** 19 537–19 563.

Constable, C.G., Parker, R.L. & Stark, P.B., 1993. Geomagnetic field models incorporating frozen-flux constraints, *Geophys. J. Int.,* **113,** 419–433.

Gubbins, D., 1984. Geomagnetic field analysis–II. Secular variation consistent with a perfectly conducting core, *Geophys. J. R. astr. Soc.,* **77,** 753–766.

Gubbins, D. & Bloxham, J., 1985. Geomagnetic field analysis—III. Magnetic fields on the core-mantle boundary, *Geophys. J. R. astr. Soc.,* **80,** 695–713.

Holme, R. & Bloxham, J., 1996. The treatment of attitude errors in satellite geomagnetic data, *Phys. Earth. Planet. Int.,* **98,** 221–233.

Jackson A., 1996. Kelvin's theorem applied to the Earth's core, *Proc. R. Soc. Lond. A,* **452,** 2195–2201.

Jackson, A., Jonkers, A.R.T. & Walker, M.R., 2000. Four centuries of geomagnetic secular variation from historical records, *Phil. Trans. R. Soc. Lon., A,* **358,** 957–990.

Lancaster, P. & Salkauskas, K., 1986. *Curve and Surface Fitting: An Introduction,* Academic Press, London.

Langel, R.A., 1987. *The main field in geomagnetism,* Vol I, J.A. Jacobs (Ed.) Academic Press, London.

Lawson, C.L. & Hanson, R.J., 1995. *Solving least squares problems, SIAM*.

O'Brien, M.S., 1996. Resolving magnetic flux patches at the surface of the core, *Geophys. Res. Lett.,* **23,** 3071–3074.

O'Brien, M.S., Constable, C.G. & Parker, R.L., 1997. Frozen-flux modelling for epochs 1915 and 1980, *Geophys. J. Int.,* **128,** 434–450.

Olsen, N. *et al.*, 2000. Oersted initial field model, *Geophys. Res. Lett.,* **27,** 3607–3610.

Parker, R.L., 1994. *Geophysical Inverse Theory*, Princeton University Press, New Jersey.

Press, W.H., Teukolsky, S.A., Vetterling, W.T. & Flannery, B.P., 1992. *Numerical Recipes in Fortran 77*. The Art of Scientific Computing, 2nd edn, CUP, Cambridge.

Rau, S., Christensen, U., Jackson, A. & Wicht, J., 2000. Core flow inversion tested with numerical dynamo models, *Geophys. J. Int.,* **141,** 485–498.

Roberts, P.H. & Scott, S., 1964. Truncation errors in the spherical harmonic analysis of the geomagnetic field and the problem of downward extrapolation, *J. Geomag. Geoelec.,* **15,** 148–160.

Roberts, P.H. & Scott, S., 1965. On analysis of the secular variation. I: a hydromagnetic constraint, *J. Geomagn. Geoelect.,* **17,** 137–151.

Roberts, P.H. & Glatzmaier, G.A., 2000. A test of the frozen-flux approximation using a new geodynamo model, *Phil. Trans. R. Soc. Lond.,* **358,** 1109–1121.

Shure, L., Parker, R.L. & Backus, G.E., 1982. Harmonic splines for geomagnetic modelling, *Phys. Earth. Planet. Int.,* **28,** 215–229.

Stark, P.B. & Parker, R.L., 1995. Bounded-variable least squares: an algorithm and applications, *Comp. Stat.,* **10,** 129–141.

Waddington, R., Gubbins, D. & Barber, N., 1995. Geomagnetic field analysis V: determining steady core flows directly from geomagnetic observations, *Geophys. J. Int.,* **122,** 326–350.

Walker, M.R. & Jackson A., 2000. Robust modelling of the Earth's magnetic field, *Geophys. J. Int.,* **143,** 799–808.

## APPENDIX

Here we explain the rules for the division of nodes into the constrained and unconstrained sets, $\mathcal{C}$ and $\mathcal{U}$, respectively, introduced briefly in Section 2.3. A certain null-flux patch has nodes interior $b_i^{(i)}$ [numbering $N^{(i)}$] and exterior $b_i^{(e)}$ [numbering $N^{(e)}$] to it—the most natural assignment of the nodes, which we implement, is that the set with the least number of nodes is interior. We only consider nodes adjacent to a NFC, and assign them to the interior or exterior sets, also ranking them in terms of their proximity to the curve. We then work through this list, beginning with the node closest to the curve, and decide if it is allowed to be free to change sign (enter set $\mathcal{U}$) based on a set of rules which ensure that the topology of the curve is preserved: in particular, we prevent a curve from disappearing altogether, or from breaking up into multiple patches. Rule 1, below, is the most important criterion; rules 2–6 are implemented to deal with patches containing only a few nodes, and are redundant if if the density of nodes is increased in the model to a suitable level. The final check (last paragraph) to prevent merging of patches always needs to be performed.

Let the node under consideration for assignment to $\mathcal{U}$ or $\mathcal{C}$ be $b_i^{(i)}$. Let $n_j^{(i)}$ and $n_j^{(e)}$ be nearest neighbours which are interior and exterior, respectively. The interior neighbours can be subdivided into boundary neighbours $n_j^{(b)}$ and hinterland neighbours $n_j^{(h)}$; a boundary neighbour is adjacent to a NFC, whereas a hinterland neighbour is not. Clearly the maximum number of boundary neighbours is five, because if a node has six boundary neighbours by definition

it is a hinterland node (not adjacent to a NFC) and does not need considering.

### 1 The rules

(i) If any $n_j^{(e)} \in \mathcal{U}$, set $b_i^{(i)} \in \mathcal{C}$; apply same logic also to external nodes $b_i^{(e)}$. This rule prevents the generation of extra patches as a result of two adjacent nodes which previously had opposite signs (NFC lies between them) swapping signs.

(ii) If $N^{(i)} = 1$ set $b_i^{(i)} \in \mathcal{C}$ (patch with only one node must be fixed to prevent patch disappearing).

(iii) If $N^{(i)} = 2$ and one node already in $\mathcal{U}$ set $b_i^{(i)} \in \mathcal{C}$ (again, prevent patch disappearing).

(iv) If $N^{(i)} = 3$ and two neighbours already in $\mathcal{U}$ set $b_i^{(i)} \in \mathcal{C}$ (all live on same triangle; three cannot be free or patch may disappear).

(v) Check against boundary neighbours and hinterland neighbours: use Table 3.

(vi) Check interior free list to see if any interior neighbours are free. This can occur because the free nodes are not adjacent to the same portion of the NFC; schematically they are of the form (where—is a NFC and x represents a free node)

```
– – – – – – – – – –
x     x     x     x
   x     x     x
– – – – – – – – – –
```

A final check now needs to be performed to prevent merging of different patches, which results from exterior nodes which are in $\mathcal{U}$ being neighbours; if both changed sign the patches would merge. We implement this using multiple passes through the list of exterior nodes in $\mathcal{U}$. At each pass, for each node in the (exterior) free list of the two patches we check to see if there are either common nodes or adjacent nodes. If so, we discard the node which is furthest from the NFC from the free list, and then repeat the pass until no nodes in $\mathcal{U}$ are adjacent and exterior. Note that we must treat the magnetic equator as special, because it is the only NFC which has nested NFCs; therefore, we must check both its interior and exterior list of free nodes to ensure that there is a fixed node between any free node associated with it and any free node associated with another curve.